The supplementary material gives additional information to:

1. Kinematic analysis and estimation of the potential failure volume
2. Characterisation of the fracture network
3. Fracture displacements
4. Measuring setup and data acquisition of electrical resistivities at the study site
5. Near-surface rock temperature measurements
6. Rock-mechanical laboratory tests
    - 6.1 Intact rock
    - 6.2 Rock joints
7. Numerical stability analysis
    - 7.1 Further assumptions for the procedure of the numerical analysis
    - 7.2 Additional sensitivity analyses of the numerical models

The following figures and tables are included in the text:

- Figure S1. Kinematic analysis of the unstable south-face of the Zugspitze summit crest for a potential plane or wedge failure.
- Figure S2. Structural features at the study site.
- Figure S3. Near-surface fracture displacements at the study site between 09/2013 and 07/2019.
- Table S1. Metadata on the instrumented temperature sensors at the Zugspitze summit ridge.
- Figure S4. Near-surface rock temperatures at the Zugspitze summit crest between 08/2015 and 08/2019.

- Figure S5. Warming behaviour of frozen dummy rock samples during simulated uniaxial compression, Brazil and ultrasonic tests.
- Figure S6: Influence of a bigger model domain and a higher disturbance factor D on the slope stability.
- Figure S7. Maximum model displacements versus slope angle for a warming rock slope above -2 °C.
- Figure S8. Maximum model displacements versus slope angle for a warming permafrost rock slope and the twofold amount of numerical cycles for each warming step.
- Figure S9. Maximum model displacements against slope angle for a warming permafrost rock slope with different levels of rock mass strength and deformability.

The following data sets are provided (as *.xlsx or *.txt files) in the zipped folder “Suppl. Material”:

- Dataset S1. Geometrical joint properties
- Dataset S2. Crack displacements at the field site
- Dataset S3. Raw data of the electrical resistivity tomography in the field
- Dataset S4: Laboratory electrical resistivity
- Dataset S5. Topography of the Zugspitze summit crest (for the ERT)
- Dataset S6. Near-surface rock temperature at the north-face and the south-face of the Zugspitze summit ridge
- Dataset S7. Laboratory dilatational wave and Poisson´s ratio
- Dataset S8. Laboratory uniaxial compressive strength
- Dataset S9. Laboratory uniaxial tensile strength
- Dataset S10. Laboratory joint wall compressive strength and joint basic friction angle
- Dataset S11. Roughness coefficient of joints at the field site
- Dataset S12. Size of samples for testing of intact rock properties
- Dataset S13. Warming pattern of frozen dummy rock cylinders / discs during simulated uniaxial compression testing / Brazil tests.
- Dataset S14. Results of the numerical model: Maximum displacements and factors of safety
- Dataset S15. Numerical codes for UDEC
- Dataset S16. Material parameters for different disturbance factors D

1 Kinematic analysis and estimation of the potential failure volume

UAV-based photogrammetry was performed at the Zugspitze summit crest to compute a 3D point cloud providing information on the possible (i) shear zones delimiting the unstable rock mass, (ii) type of failure and (iii) failure volume. Data were acquired with the drone Phantom 4 Pro (DJI). Red, green and blue images are captured simultaneously and with different viewing angles. The included camera is equipped with a 1”CMOS sensor with 20 MP. The 3D point cloud was generated with Agisoft Photoscan v.1.4.5 and analysed with RISCAN PRO 2.7.1 64 bit. It has a total number of 21 Mio points with a resolution of ca. 5 cm, and rgb information for identifying geological features.

Shear zones SZ1, SZ2 and SZ3, which were identified as potential failure planes in the field (Fig. 1e), were recognised in the 3D point cloud by manually defining sections of points which lie on a common plane. These sections were extrapolated to mean failure planes and intersect with each other and the slope face. A fourth and fifth shear zone (SZ4 and SZ5) were determined to form the possible downslope boundary of the unstable rock mass (Fig. 1e). The approximate total volume of the potentially failing rock mass was estimated to be $2.9 * 10^4$ m³. This was done by calculating the difference between the intersected failure planes and the terrain surface, both related to a lower reference plane.

A kinematic analysis of a potential plane and wedge failure was conducted with DIPS 7.0 including the southern slope-face (45/160) and the main shear zones, which were identified due to field mapping and the preceding analysis of the point cloud. The lateral limit for critical dip directions of the failure plane was set to the default of 20°. The friction angle was set to 30°, based on direct shear tests of frozen and unfrozen Wetterstein limestone by Krautblatter et al. (2013).

The results showed that pure plane failure can occur for those sections of SZ1, SZ4 or SZ5 for which the dip is lower than the inclination of the slope-face (45°) and higher than the friction angle of the rock joints (30°) (Fig. S1a). Pure wedge failure is possible for intersections of SZ3/SZ5, and marginally for SZ3/SZ4 or SZ3/SZ1 (Fig. S1b). Though planar sliding is the dominant kinematic failure mode which affects the major left part of the unstable rock mass, we assume that the instability is driven by a complex combination of both a plane and a wedge failure (Fig. 1e, Fig. S1). Neither pure planar sliding nor pure wedge sliding are likely to be the controlling failure mechanism. In the upper part of the rock slope, planar sliding may occur along SZ1, while wedge failure supports the displacement along SZ1/SZ3 including a tension crack SZ2. At lower slope sections, planar sliding can occur along SZ4 and SZ5, while wedge failure potentially enhances the failure process along SZ3 and a stepped plane constituted of SZ4 and SZ5.

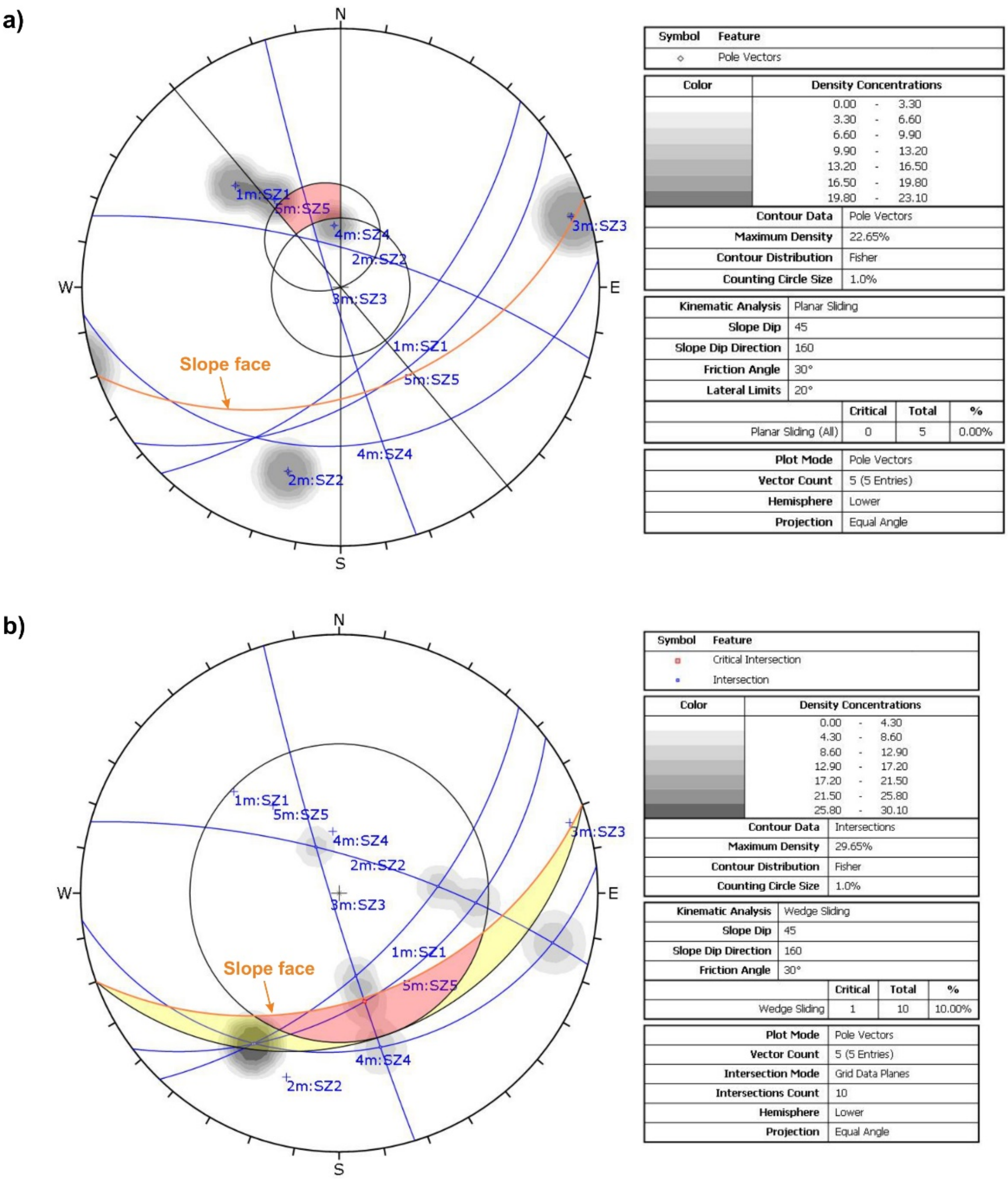

Figure S1: Kinematic analysis of the unstable south-face of the Zugspitze summit crest for a potential plane or wedge failure. (a) Plane failure can occur for those shear zones whose poles lie within the critical red window. This is valid for SZ4 and SZ5, and marginally for SZ1. The friction cone in the centre has an angle of 30°. The lateral limit of the critical window is set to 20°. (b) Wedge failure is possible for intersections of planes which lie within the critical red window. This is the case for intersections of SZ3/SZ5, and marginally for SZ3/SZ4 or SZ3/SZ1. Sliding along SZ4 can occur for wedges constituted of SZ1/SZ4 or SZ5/SZ4 (yellow area). The friction cone at the margin has an angle of 30°.

2 Characterisation of the fracture network

The fracture network was mapped systematically along five distinct scanlines distributed over the south-slope and at the top of the summit crest (Fig. 1b) as working at the north-face requires rope safeguarding. The studied joint characteristics involved dip and dip direction, spacing, aperture, joint frequency and joint roughness (Table 2). The entire data set contains 129 discontinuities.

The mean dip and dip direction of the joint sets were calculated with DIPS 7.0 (RocScience) defining main joint sets in pole density plots. Geometrical Terzaghi weighting was applied to correct potential bias which is introduced in favour of discontinuities perpendicular to the direction of the scanline.

The joint roughness was recorded with a Barton comb / profilometer along 14 profiles not included in the five scanlines. Each profile consisted of between three and seven subsections of 26 cm. Data acquisition and analysis were performed according to Tse and Cruden (1979). The coefficient Z_2 was determined by

$$Z_2 = [\frac{1}{M(\Delta x)^2} \sum_{i=1}^{M} (yi + 1 - \ yi)^2]^{1/2} \qquad \text{(S1)}$$

where y_i is the distance between the rock surface and a fixed reference line, x is a specified equal record interval and M is the number of measured intervals along the profile. The applied sampling interval x at the field site was 5 mm. To calculate the JRC, the following formula proposed by Yang et al. (2001) was used:

$$JRC = 32.69 + 32.98\ log_{10}\ Z_2 \qquad \text{(S2)}$$

As Z_2 is only valid for the range of 0.1 to 0.42, values < 0.1 were assigned a zero JRC.

A very prominent and persistent shear zone was detected at the south-slope (SZ1 in Fig. 1). According to geotechnical field mapping, SZ1 has a trace length of approximately 70 m and runs in a maximum depth of 10–15 m. At some places it opens to a decimetre wide, highly fractured zone filled with fine material ranging from clay-size to gravel-size. This type of infilling is observed in most of the bigger shear zones at the summit region (Fig. S2c). Four dolines develop along the major shear zones SZ1 and SZ2 (Fig. 1a): Two of them form along SZ1, while the third one develops along SZ2. The fourth doline is located at the point of intersection between SZ1 and SZ2 (Fig. S2a and Fig. S2b).

Figure S2: Growing doline at the crestline of the Zugspitze summit, at the intersection of SZ1 and SZ2 (a) in 2009 and (b) in 2018. (c) Shear zone filled with fine material.

3 Fracture displacements

We performed repeated recordings of crack displacements distributed over the most active parts of the rockslide at the Zugspitze summit crest to quantify mean displacement rates and assess seasonal patterns of movement. The upper part of the south-face was equipped with 32 sections for displacement measurements. Each section is delimited by two plugs fixed in the rock crossing one or more important joints or shear zones. Values were collected with a digital tape extensometer (Soil Instruments Ltd.) at the beginning (June/July) and at the end (September/October) of the accessible, snow-free summer season between 09/2013 and 07/2019. The tape extensometer measures with a maximum resolution of 0.01 mm. The locations of the sections are displayed in Fig. 1b.

The annual mean absolute displacement for the period 09/2013–07/2019 measures 2.1 mm y^{-1} (Fig. S3a). To study the evolution of displacements over time, absolute annual fracture displacement rates were calculated from early summer to early summer of the subsequent year. Here, the medians of annual displacements range between 0.3 and 4.8 mm y^{-1} and do not point to either an acceleration or a deceleration between 2013 and 2019. Recording crack displacements twice a year, at the beginning and at the end of the summer season, allowed us to compare summer displacement rates with those of the remaining year (Fig. S3b): The monthly mean displacement rate reduces by a factor of 6.4 when changing from summer to the remaining seasons (summer: 0.63 mm mo^{-1}; remaining year: 0.10 mm mo^{-1}). This corresponds to a decrease by 84.4 %.

a)

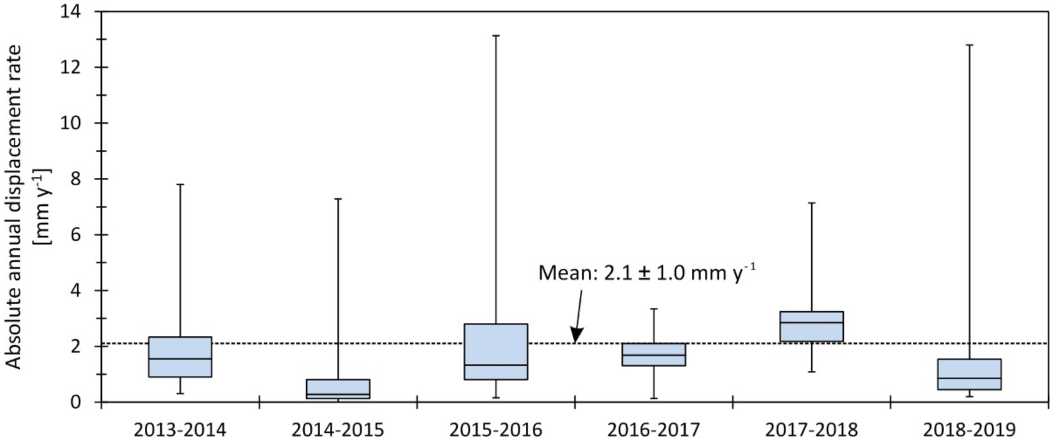

b)

	Fracture displacement in summer [mm mo^{-1}] 2015	2016	2017	2018	Total
Mean	1,22	0,21	0,85	0,25	0,63
Standard deviation	1,45	0,15	0,39	0,50	
Number of measured sections	30	30	31	30	

	in the remaining year [mm mo^{-1}] 2015/16	2016/17	2017/18	2018/19	Total
Mean	0,05	0,13	0,04	0,09	0,10
Standard deviation	0,04	0,07	0,04	0,15	
Number of measured sections	31	31	30	31	

Figure S3: Near-surface fracture displacements at the south-face of the Zugspitze summit crest between 09/2013 and 07/2019. (a) Boxplot of annual absolute displacement rates for the time period 2013-2019. (b) Monthly rates for summer (June to September) and the remaining year (October to May) since 2015.

4 Measuring setup and data acquisition of electrical resistivities at the study site

ERT was applied along a transect of approximately 100 m, crossing the ridge and covering its north- and south-face (Fig. 1a, Fig. 1b). In this way, we could assess more properly the effect of thermal differences induced by various expositions at the crest-topography. The transect for ERT consists of 41 electrodes (stainless steel nails) which were installed once and used for both surveys. The electrodes were separated from each other by a mean spacing of 2.5 m. To enhance electrode coupling, the steel nails were greased with an electrically conductive fluid and water was added to the contact between nails and ground just before the survey. Acquisition of geoelectrical data was performed with two distinct devices: an ABEM Terrameter SAS 1000 and a Terrameter LS with maximum input/output voltages of ± 400 and ± 600 V, respectively, and corresponding injected currents of 1 and 0.1 mA, respectively. The applied input/output voltage and the current were standardised for all surveys and were 500 V and 1 mA, respectively. The applied electrode configurations for the ER surveys were Wenner (in 2014) and Wenner-Schlumberger (in 2015). 2D data processing and inversions were performed with the commercial software package Res2Dinv. Data inversions were performed using robust inversion and model refinement with half the unit electrode spacing (Loke, 2019).

5 Near-surface rock temperature

Rock temperature sensors (Maxim Integrated, iButton model DS1922L-F5) were instrumented in the direct surroundings of the geophysical survey lines in depths of 10 and 80 cm (locations are displayed in Fig. 1b). So far, iButtons have been applied successfully to measure ground surface or bedrock temperatures in alpine terrain (Gubler et al., 2011; Keuschnig, 2016). The preparation of the sensors and the installation technique in solid rock were taken from Keuschnig (2016). The sensors measured the rock temperature every two hours between August of 2015 to August of 2019 with an accuracy of ± 0.5 °C. Five iButtons were installed at the north-face and five iButtons at the south-face, whilst two of them were located within the shear zone SZ1 (Table S1). The recordings of the thermistors demonstrate that the surficial rock layer (< 1 m) thaws during the summer months. This is valid for both slope-faces of the summit ridge (Fig. S4).

Table S1: Metadata on the instrumented temperature sensors at the Zugspitze summit ridge. Locations are given in Fig. 1b.

iButton	Aspect [°]	Slope [°]	Depth [cm]	Characteristics
1	210 (S)	24	10	often snow, intense solar radiation
2	320 (N)	70	10	thin snow cover, shaded
3	320 (N)	70	10	thin snow cover, shaded
4	320 (N)	60	10	thin snow cover, shaded
5	320 (N)	52	10	thin snow cover, shaded
6	320 (N)	70	80	thin snow cover, shaded
7	160 (S)	32	10	often snow, intense solar radiation
8	140 (S)	55	10	at SZ1, often snow, intense solar radiation
9	160 (S)	58	10	often snow, intense solar radiation
10	140 (S)	55	75	at SZ1, often snow, intense solar radiation

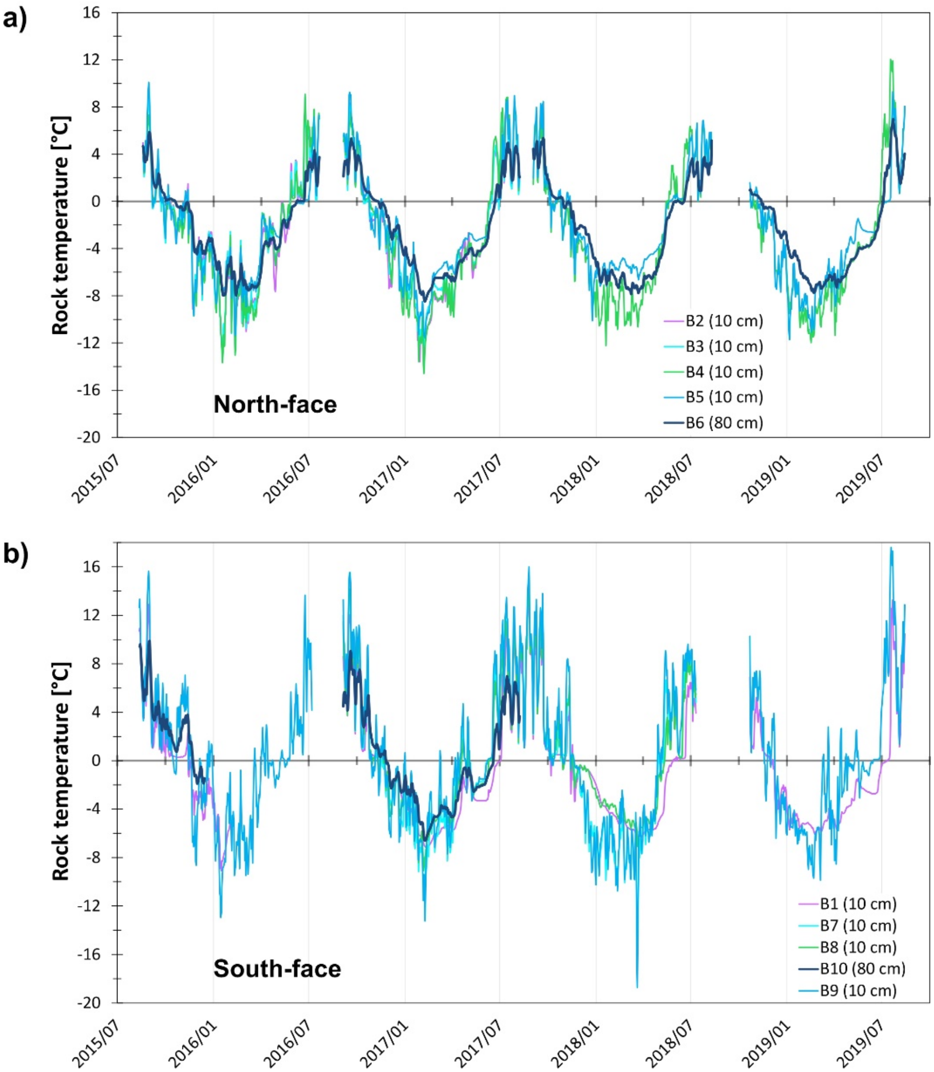

Figure S4: Near-surface rock temperatures measured in a depth of 10-80 cm at the Zugspitze summit crest between 08/2015 and 08/2019: (a) north-face, (b) south-face.

6 Rock-mechanical laboratory tests

6.1 Intact rock

6.1.1 Preparation of the rock samples

The rock samples for the laboratory tests were cored from Wetterstein limestone blocks with a mean side length of 0.4 ± 0.1 m that were picked from the study site and the lower Zugspitzplatt (2590 m a.s.l.; Fig. 1a). Uniaxial compression and Brazil tests were conducted in accordance with the recommendations of the Commission on Rock Testing of the German Geotechnical Society (Lepique, 2008; Mutschler, 2004). Ultrasonic tests were performed in accordance with the norm on Non-destructive testing of the European Committee for Standardization (DIN EN ISO 16810, 2014). The rock cores of 51 ± 0.1 mm diameter were cut with a diamond saw into 103 ± 1 mm thick cylinders for the uniaxial compression and ultrasonic tests and into 25 ± 1 mm thick discs for the Brazil tests. The high structural isotropy of the Wetterstein limestone allowed us to ignore any specific drilling orientation dependent on bedding or foliation.

We assume the rock mass of a real-world rock slope to be close to a saturated state. Therefore, we tested the rock samples in a frozen saturated and unfrozen saturated condition. For this, they were kept in a water bath for at least 48 h (DIN EN ISO 13755, 2002). The samples were regarded as nearly saturated when successive mass determinations yielded values varying less than 0.1 %. Frozen conditions were achieved by freezing saturated rock cores at -28 °C in a cooling box for at least 48 h. A natural rock slope is expected to be nearly water-saturated for the following reasons: (i) While near surface rock saturation fluctuates highly due to meteorological influences like precipitation, wind or insulation, the rock moisture in depths greater than 15 cm remains unchanged; here, it ranges between approximately 75 and 90 % dependent on the rock type and its porosity (Rode et al., 2016; Sass, 2005). (ii) The successful application of ER surveying in permafrost bedrock in the presented study (Section 2.1.2) and in many others confirm that the investigated rock slopes are saturated, since this technique only works well in saturated rock: (a) In rocks with a high degree of water saturation, electric current can be propagated due to electrolytic conduction. The DC conductivity of porous or fractured subsurface matter highly depends on saturation of the pore space and conductivity of the pore fluid (Supper et al., 2014; Telford et al., 1990). (b) The detected large ranges in electrical resistivity indicate a high degree of water saturation, since only water-saturated rocks can show a significant difference in conductivity/electrical resistivity when switching from the unfrozen to the frozen state, or vice versa (e.g. Mellor, 1973). Accordingly, water-saturated rock samples are recommended to be used for the laboratory calibration of the electrical resistivity of frozen and unfrozen rock for ERT in rock walls (Krautblatter et al., 2010).

6.1.2 Test setups

As the testing instruments were not located in a cooled room, the frozen rock samples warmed during the tests. However, for determination of frozen mechanical properties, the rock specimens had to remain frozen during the whole experiments. Thus, the rock discs during Brazil tests were isolated with a polystyrene box which did not affect the progress of the tests (Fig. S5d). Isolation of the rock cylinders could not be realised as the box would prevent the measurement of axial and diametric strain during uniaxial compression and the measurement of dilatational waves during ultrasonic testing.

Hence, we additionally simulated a series of pretests to carefully observe the warming behaviour of dummy rock samples during typical uniaxial compression and Brazilian tests. The warming of rock cylinders during ultrasonic testing was assumed to behave in the same way as in uniaxial compression. As a result, the pretests of the latter were taken as representative for warming during ultrasonic tests. Warming was monitored by Pt100 temperature sensors (Greisinger GMH3750, with a 0.03 °C precision) inserted in the centre and close to the end of the rock sample (Fig. S5b and Fig. S5d). A pretest consisted in fitting the dummy sample into the apparatus and monitor the progress of warming inside the rock specimens until they were thawed.

A negligible load was applied to the samples to prevent the destruction of the thermistors or a potential weakening of the sample due to the drilled holes.

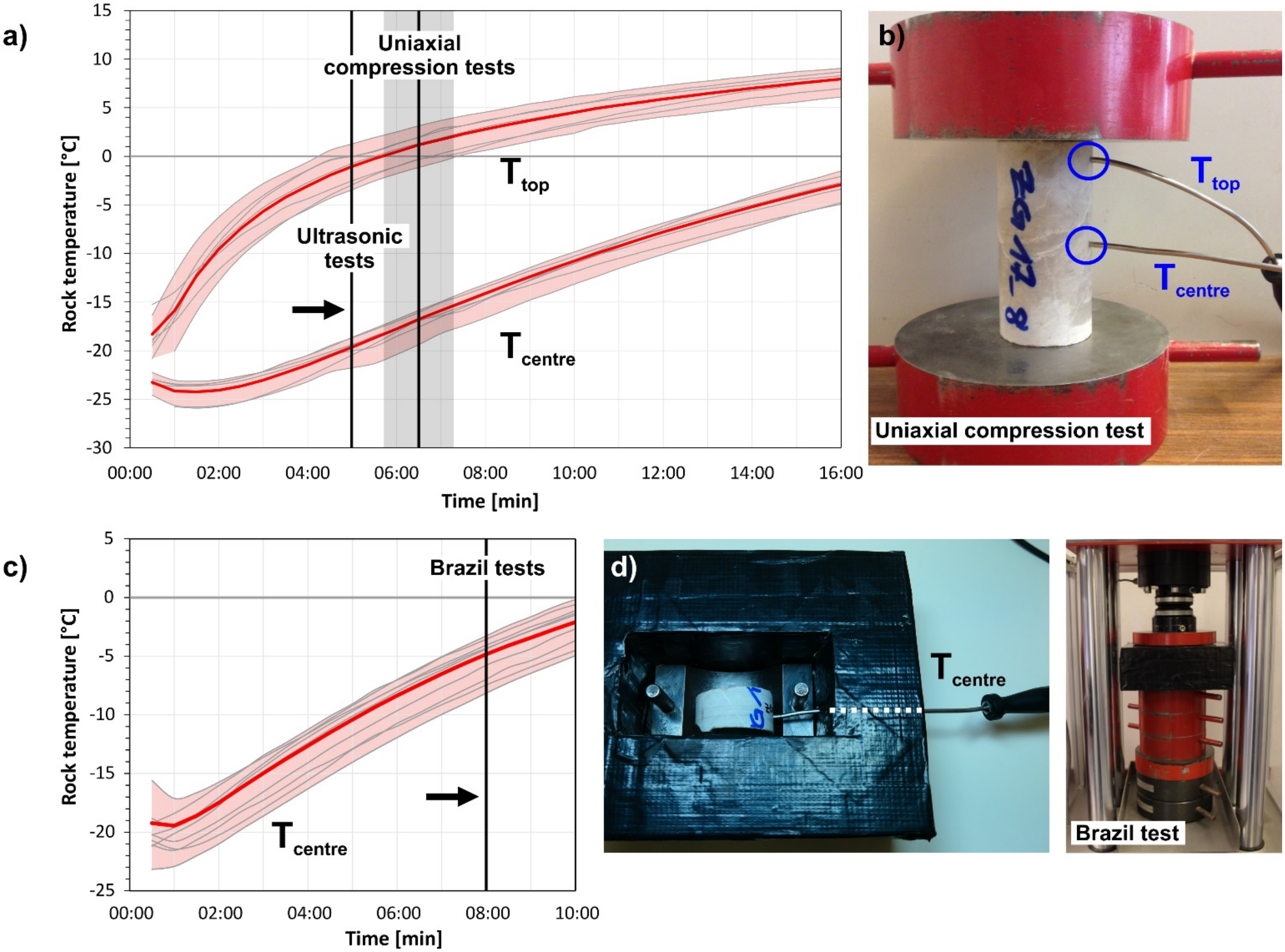

Figure S5: (a) Warming pattern for frozen dummy rock cylinders with two thermistors during simulated uniaxial compression testing. (b) Rock cylinder mounted between loading plates that are used in a typical uniaxial compression test. (c) Warming curves for frozen dummy rock discs with one central thermistor during simulated Brazil tests. (d) Isolation of a rock disc during pretests with temperature logging (left) and a typical Brazil test (right). Black lines = Maximum duration of mechanical tests. Black line with grey area = Mean duration of compression tests with standard deviation. Red thick line = Mean rock temperature during pretests. Red area = Range of variation of warming curves during pretests.

6.1.3 Testing conditions

Overall, we performed 28 uniaxial compression tests (14 unfrozen, 14 frozen), 60 Brazil tests (30 unfrozen, 30 frozen), 60 ultrasonic tests (30 unfrozen, 30 frozen) and 90 density tests (60 with the discs and 30 with the cylinders):

- Uniaxial compression tests were performed to provide data on the uniaxial compressive stress at failure. Tests were run with a ToniNorm compression testing machine (DIN EN ISO 7500-1, 2018). A constant strain of 0.6 mm / (m $*$ min) was applied to the samples provoking failure within 8 min.
- Brazil tests were conducted to collect data on the indirect tensile stress at failure which is the tensile stress normal to the uniaxially loaded areas of the specimen. A ToniNorm tension testing machine according to the (DIN EN ISO 7500-1, 2018) was used to apply a load at a constant rate of 70 N/s, leading to failure within 6 min.
- Ultrasonic tests were run to determine the velocity of the dilatational wave propagating through the specimen. The apparatus consisted of a signal generator USG40, a transmitter type UPG 250, a receiver type UPE and a preamplifier VV41 by Geotron Electronics. The rock samples were fixed between the piezoelectric transducer pair at the centres of the flat contact surfaces. Any water film at the contact surfaces of the rock cylinders was removed before testing with an absorbent cloth. Measurements were run with a frequency of 20kHz.
- The rock density ρ was defined due to weighing in an immersion bath following the standard procedure of the (DIN EN ISO 1097-6, 2005).

The test durations, provided by the black lines in Fig. S5a and Fig. S5c, also include the mounting of the samples into the apparatus: uniaxial compression tests had a mean duration of 6.5 ± 0.8 min, while Brazil tests and ultrasonic tests did not exceed 8 and 5 min, respectively. Hereafter, rock temperatures in the centre of the samples lay below -5 °C during Brazil tests, below -15 °C during uniaxial compression tests and below -20 °C during ultrasonic tests. As such, we could guarantee frozen conditions for the Brazil and the ultrasonic tests, while the major central part of the cylinders in the uniaxial compression tests were frozen, too. Unfrozen mechanical properties were studied at room temperature.

6.2 Rock joints

The residual friction angle ϕ_r was estimated according to (Barton and Choubey, 1977), using the basic friction angle ϕ_b as well as the Schmidt hammer rebound hardness R and r for unweathered, sawn surfaces and weathered surfaces, respectively.

6.2.1 Preparation of the rock samples

For the basic friction angle of the rock joints, we performed tilt tests with unweathered sawn rock surfaces of frozen and unfrozen Wetterstein limestone following the procedure suggested by Barton and Choubey (1977) and Barton (2013). For the Schmidt hammer rebound hardnesses R and r, we conducted a series of Schmidt hammer tests in the laboratory with dry unweathered sawn and wet weathered rock surfaces of frozen and unfrozen Wetterstein limestone. The tests were prepared and realised following the proposed procedure of the International Society for Rock Mechanics (ISRM; Ulusay, 2015) and Aydin et al. (2005).

The rock samples were cored from Wetterstein limestone blocks with a mean side length of 0.4 ± 0.1 m that were picked from the study site (Fig. 1) or the lower Zugspitzplatt (2590 m a.s.l.). The rock cores were cut with a diamond saw into 10 cylinders for the tilt tests, while two of them were taken for testing the Schmidt hammer rebound hardness R. The samples for the tilt tests had a mean height of 83.1 ± 2.6 mm and the samples for the Schmidt hammer tests on unweathered joint surfaces had a mean height of 84.1 mm. The corresponding mean diameters ranged between 148.5 ± 0.2 and 148.6 mm, respectively. The wet weathered joint surfaces (for determining r) were tested at a single Wetterstein limestone block with a volume of 0.02 m^3, collected from the Zugspitze summit ridge.

6.2.2 Test setups and procedures

Unfrozen conditions corresponded to ambient room temperature. Frozen conditions for the tilt tests and the Schmidt hammer tests on unweathered joint surfaces were achieved by storing the rock specimens in a cooling box at -28 °C for 48 h. The bigger block for the Schmidt hammer tests on wet weathered joint surfaces were stored for 48 h in a bigger, self-constructed and isolated cooling box at -10 °C. The samples were tested directly after taking them out of the cooling box. As the experiments did not exceed 2-4 min, we could guarantee the rock samples to be frozen during the tests. Isolation of the specimens during the tests was technically not feasible. Any ice layer that could have developed at the rock surfaces during freezing was carefully removed before testing to prevent a potential influence on the results.

According to the ISRM (Ulusay, 2015), samples for Schmidt hammer tests have to be firmly fixed to a heavy steel base or a firm and flat ground to avoid a potential loss of impact energy. The big rock block was too heavy to move during the tests. However, the smaller and lighter rock cylinders (for determining R) were mounted with their flat ends between two load platens of a ToniNorm uniaxial compression machine (with a maximum applicable load of 250 kN). After that, the samples were firmly fixed by applying an axial load of 60 N.

A Schmidt hammer of the N-type was used for testing the rebound hardness. For the unweathered surfaces, the impacts by the plunger tip of the hammer were applied to the rounded smooth sides of the cylinders. The impacts were distributed along the cylinder sides by rotating it on the flat ends in steps of 90°. The weathered surface of the bigger rock block was sampled on two faces of the specimen. We collected at least 20 impact readings per specimen and averaged the upper 50 %. Rebound values collected in down- or upward direction were normalised in accordance with the ISRM standard (Ulusay, 2015).

The weathered surface of the rock block was characterised by a higher roughness and small asperities which got partly destroyed by the hammer impacts. This led to a higher variation in the data.

7 Numerical stability analysis

7.1 Further assumptions for the procedure of the numerical analysis

The general modelling procedure consists of four steps: the calculation of an initial equilibrium and three successive steps of potential destabilisation which include the progressive destruction of intact rock bridges, the warming and the thawing of a permafrost rock slope. The past destruction of cohesive intact rock bridges was simulated by a reduction of the apparent joint cohesion and friction angle in three steps which represents a progressive increase of the joint persistence from 30 to 90 % (Stages 1–4 in Table 6, Table 7). This procedure simulates "step-path" failure on the slope scale in a simplified way which is characterised by the interconnection of pre-existing, adjacent discontinuities through intact rock bridges (Eberhardt et al., 2004; Huang et al., 2015; Mejía Camones et al., 2013). The reduction in the shear strength involves processes of stress concentration, crack initiation, crack propagation and coalescence, slip weakening and the formation of a continuous failure plane or zone (Zhang et al., 2015), which were not numerically modelled as this would be beyond the scope of this study. The presented model of the Zugspitze ridge considers crack coalescence to occur by shear and tensile mode or a tensile-shear combination, which has been observed on the micro-scale by Zhang and Wong (2013). The resulting new connections can form coplanar or oblique to the pre-existing joints (Huang et al., 2015). At the scale of the Zugspitze ridge, we assume the joint sets K1, K3 and K4 to link in both coplanar and oblique form, leading to the formation of straight or stepped failure planes.

7.2 Additional sensitivity analyses of the numerical models

To analyse the influence of a higher disturbance factor D on the stability of the Zugspitze summit crest, D was changed to a maximum of 1. Accordingly, the mechanical parameters G, K, σ_{tm}, k_n and k_s reduced by a mean of 56 %. While the model results showed higher displacements, the factor of safety remained unchanged (Fig. S6). Further, we extended the model domain by 20 m to the right/south and by 20 m downward to test if the model results are affected by a bigger model domain which ends in a flatter slope (Domain B in Fig. S6). Again, the model results demonstrated that the overall stability of the slope does not change, although the displacements are higher by a factor of 1 to 3.

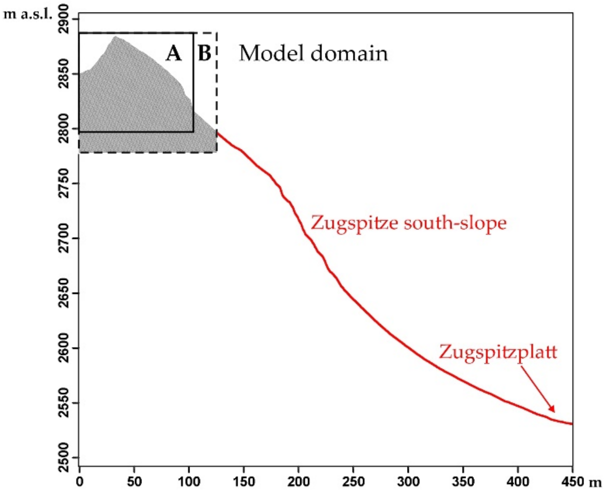

		Principal modelling steps	Initial state	Progressive destruction of rock bridges			Stepwise warming from surface to core				
		Model stage number	1	2	3	4	5	6	7	8	9
Max displ. [mm]	Model domain size	A (D = 0)	7,6	7,8	7,8	7,7	7,7	7,7	7,8	7,9	8,2
		B	23,8	24,0	24,0	26,1	26,2	26,2	26,1	26,2	27,3
	Disturbance factor	D = 1	18,2	19,5	19,5	19,4	19,4	19,5	17,9	18,9	19,1
FoS	Model domain size	A (D = 0)	10,9			2,6	3,4				1,3
		B	9,1		4,6	2,2	2,8				1,1
	Disturbance factor	D = 1	10,7			2,6	3,4				1,3

		Principal modelling steps	Stepwise thawing from surface to core					All unfrozen
		Model stage number	10	11	12	13	14	15
Max displ. [mm]	Model domain size	A (D = 0)	141,1	419,5	520,4	616,8	689,7	776,3
		B	107,3	316,7	671,0	1066,4	1192,0	1226,4
	Disturbance factor	D = 1	273,2	782,3	1085,0	1232,7	1327,0	1407,7
FoS	Model domain size	A (D = 0)	0,6	0,6				0,6
		B	0,5	0,6				0,7
	Disturbance factor	D = 1	0,6	0,7				0,7

Figure S6: Influence of a bigger model domain and a higher disturbance factor D on the slope stability. Model domain A and D = 0 were used for the original Zugspitze model (Section 2). The topography of the Zugspitze (red line) was extracted from a digital elevation model in ArcGIS.

All numerical stability analyses for progressive warming were started with a frozen rock slope at a temperature of -4 °C. The stability calculations of the universal model were additionally run with a start temperature of -2 °C to be able to estimate the effect of a higher start temperature on the model results as material parameters with a lower strength have been assigned for the calculation of the initial equilibrium. However, the additional model runs led to similar displacement magnitudes as for a modelling start at -4 °C (Fig. S7): the slope-dependent pattern is generally the same with two onsets of initiating instability at slope gradients of above 50 or 55° (transition to Domain 2) and a slope gradient above 62° (transition to Domain 3).

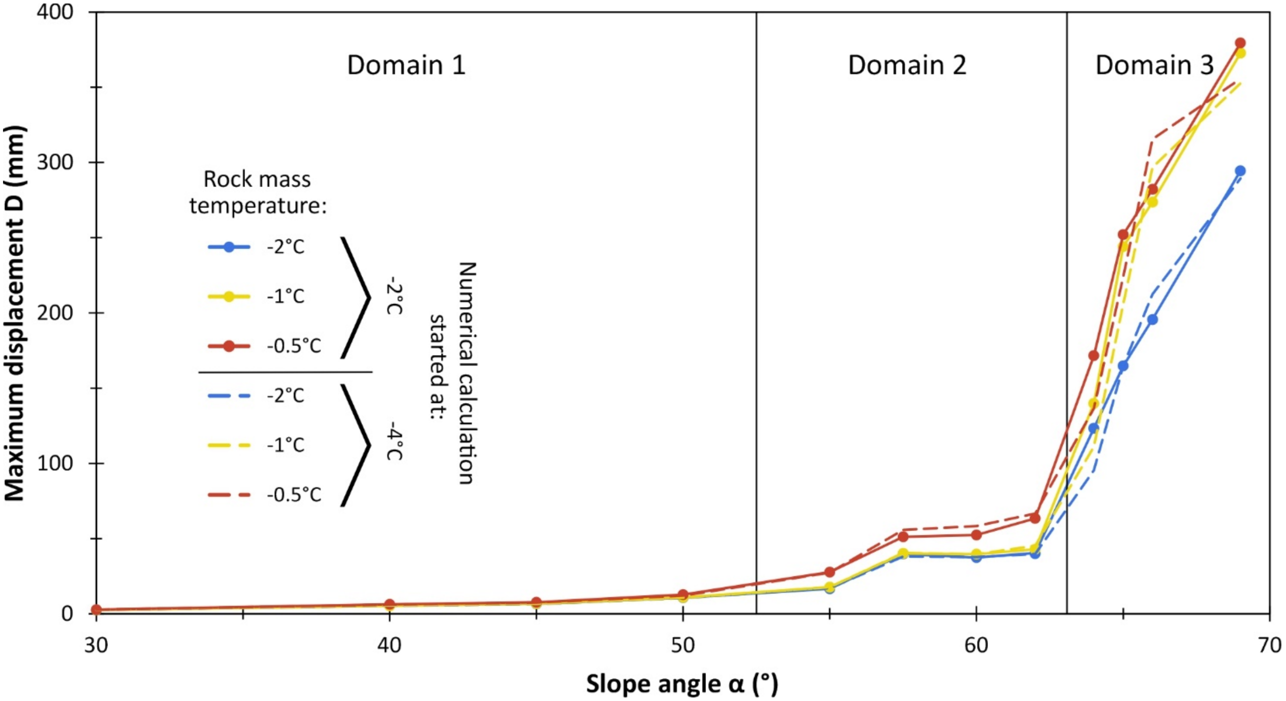

Figure S7: Maximum block and zone model displacements versus slope gradient for a permafrost rock slope at -2, -1 and -0.5 °C. Solid lines with circles represent numerical results of calculations started at -2 °C, while dashed lines represent numerical results of calculations started at -4 °C (according to Fig. 8). The three domains relate to a distinct displacement behaviour and are in accordance with the domains presented in Fig. 8a.

The progressive warming steps for the universal rock slope were remodeled with twice the amount of cycles to assess the effect of longer numerical computation on the mechanical response of the system. Overall, the slope-dependent pattern remains generally the same with two onsets of initiating slope instability at 50 and at 62° (Fig. S8). For warming steps between -4 and -2 °C the rock slope responded similar to the previous calculations with 3000 cycles (dashed lines). However, a warming to -1 or -0.5 °C in rock slopes with an inclination of higher than 60° resulted in displacements 10–111 % higher than in the model runs with 3000 cycles. However, the displacements remained within the same order of magnitude.

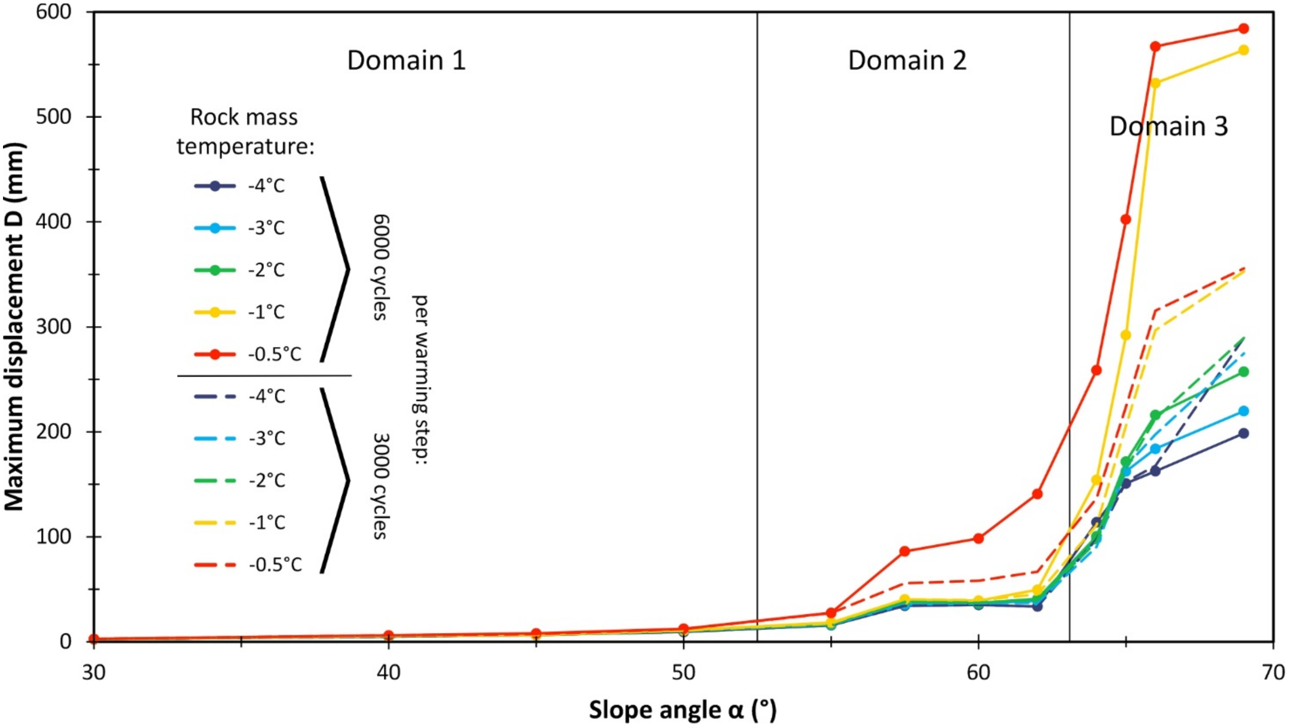

Figure S8: Maximum displacements against slope angle for a permafrost rock slope at temperatures between -4 and -0.5 °C. Dashed lines represent warming steps with 3000 cycles (according to Fig. 8), while solid lines with circles represent warming steps with the twofold amount of numerical cycles (6000). The three domains relate to a distinct displacement behaviour and are in accordance with the domains presented in Fig. 8a.

The results of the sensitivity analysis with input data from the Zugspitze summit ridge (Sect. 4.2) are valid for warming permafrost rock slopes which consist of limestone, with strength and deformability similar to the Wetterstein limestone tested in this study. A transfer to permafrost rock slopes with a different lithology requires more modelling, as the mechanical parameters of the rock mass vary among different rock types and may lead to different model results. To get an impression of this effect, we performed a couple of model test runs with varying values of the mechanical rock mass properties ranging from very low to unrealistically high. However, the selected range of the implemented mechanical properties also covers typical values of a wide range of different rock types (Clauser and Huenges, 1995; Kulatilake et al., 1992; Schön, 2015). We defined four fictitious levels of rock mass strength and deformability which are lower than the one of the Wetterstein limestone used for the simplified model (Sect. 4.2), and six fictitious levels which are higher (Fig. S9b). Modelling was performed for a rock slope with an inclination of 60° and a mean temperature of -4 °C. In a second step, we examined the pattern of displacements over the full range of slope gradients (30-66°) and temperatures (-0.5 to -4 °C) of the simplified model using a further specific level of high strength (Level 5) for a new set of model runs (Fig. S9a).

The results of the analysis showed that the displacements mostly remained within the same order of magnitude (Fig. S9a). This is valid for the model runs with (i) varying strength and deformability at a slope angle of 60° and a temperature of -4 °C (results lie within the dashed blue box), and (ii) the specific strength and deformability level 5 over the entire range of slope angles and temperatures of the simplified model.

a)

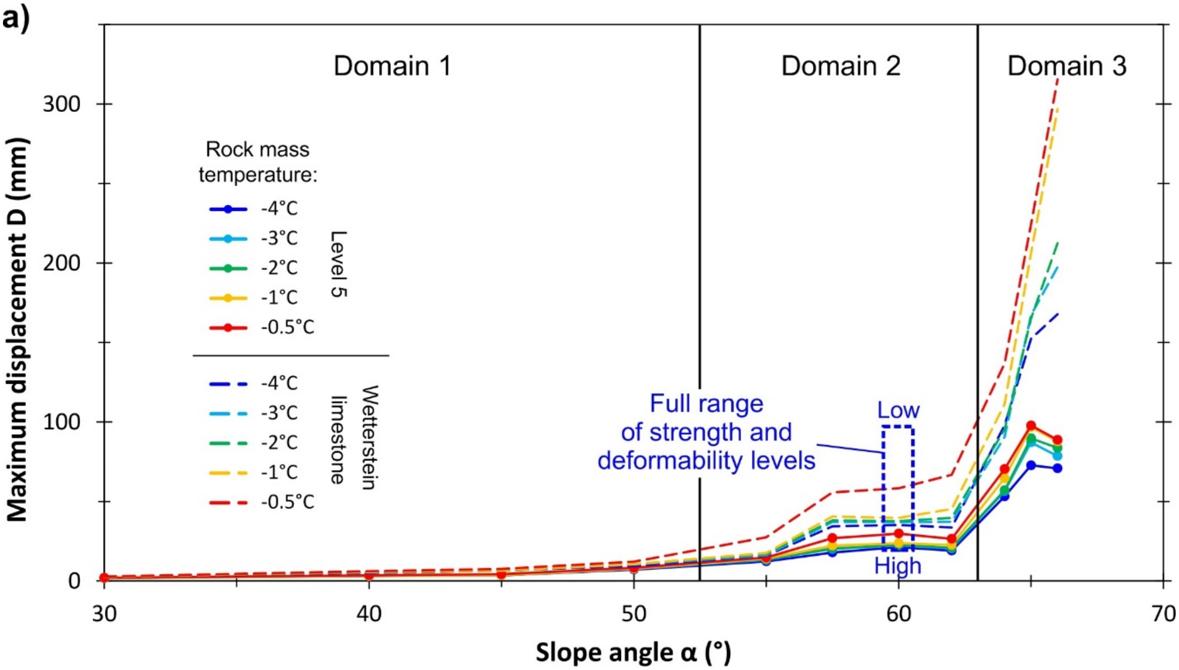

b)

	Strength and deformability level of the rock mass	ρ [g/cm^3]	K_m [GPa]	G_m [GPa]	c_m [MPa]	σ_{tm} [MPa]	φ_m [°]
		Mechanical parameter					
Low	-4	2,4	2,5	1,25	0,5	0,125	20
	-3	2,5	5	2,5	1	0,25	30
	-2	2,6	10	5	2	0,5	36
	-1	2,7	15	7,5	3	0,75	42
	0 (Wetterstein limestone: model)	2,7	20,6	9,52	4	0,9	44
	1	2,7	30	14	6	1,5	46
	2	2,7	41	19	8	2	46
	3	2,8	82	38	16	4	49
	4	2,9	164	76	32	8	52
	5 (used for model runs at temperatures from -4 to -0.5°C and slope angles from 30 to 66°)	2,7	200	90	40	9	55
	6	3,0	328	152	64	16	55
High	7	3,1	656	304	128	32	59

Figure S9: (a) Maximum block and zone model displacements versus slope angle for different fictitious levels of rock mass strength and deformability and for temperatures between -4 and -0.5 °C. Dashed lines represent calculations with Wetterstein limestone (according to Fig. 8), while solid lines with circles represent calculations with a rock type that has a strength and deformability one order of magnitude higher. The dashed blue box defines the range of displacements for all rock mass levels presented in (b), at -4 °C and for a slope gradient of 60°. (b) Mechanical parameters for the distinct rock masses with varying strength and deformability.

References

Aydin, A., and Basu, A.: The Schmidt hammer in rock material characterization, Eng. Geol., 81, 1–14, 2005.

Barton, N. R.: Shear strength criteria for rock, rock joints, rockfill and rock masses: Problems and some solutions, J. Rock Mech. Geotech. Eng., 5, 249–261, https://doi.org/10.1016/j.jrmge.2013.05.008, 2013.

Barton, N. R. and Choubey, V.: The shear strength of rock joints in theory and practice, Rock Mech., 10, 1–54, 1977.

Clauser, C. and Huenges, E.: Thermal conductivity of rocks and minerals, in: Rock Physics & Phase Relations: A Handbook of Physical Constants, American Geophysical Union, Washington, D. C., 105–126, 1995.

DIN EN ISO 1097-6: Tests for mechanical and physical properties of aggregates - Part 6: Determination of particle density and water absorption; German version EN 1097-6:2000, 91.100.15, Beuth Verlag GmbH, Berlin, 2005.

DIN EN ISO 13755: Natural stone test methods - Determination of water absorption at atmospheric pressure; German version EN 13755: 2001, 73.020, Beuth Verlag GmbH, Berlin, 2002.

DIN EN ISO 16810: Non-destructive testing - Ultrasonic testing - General principles (ISO 16810: 2012); German version EN ISO 16810: 2014, 19.100, Beuth Verlag GmbH, Berlin, 2014.

DIN EN ISO 7500-1: Metallic materials - Calibration and verification of static uniaxial testing machines - Part 1: Tension/compression testing machines - Calibration and verification of the force-measuring system, Beuth Verlag GmbH, Berlin, 2018.

Eberhardt, E., Stead, D. and Coggan, J. S.: Numerical analysis of initiation and progressive failure in natural rock slopes—the 1991 Randa rockslide, Int. J. Rock Mech. Min., 41, 69–87, https://doi.org/10.1016/S1365-1609(03)00076-5, 2004.

Gubler, S., Fiddes, J., Keller, M. and Gruber, S.: Scale-dependent measurement and analysis of ground surface temperature variability in alpine terrain, The Cryosphere, 5, 431–443, https://doi.org/10.5194/tc-5-431-2011, 2011.

Huang, D., Cen, D., Ma, G. and Huang, R.: Step-path failure of rock slopes with intermittent joints, Landslides, 12, 911–926, https://doi.org/10.1007/s10346-014-0517-6, 2015.

Keuschnig, M.: Long-term monitoring of permafrost-affected rock walls. Towards an automatic, continuous electrical resistivity tomography (AERT) monitoring for early warning systems, Dissertation, Technical University of Munich, Munich, 2016.

Krautblatter, M., Verleysdonk, S., Flores-Orozco, A. and Kemna, A.: Temperature-calibrated imaging of seasonal changes in permafrost rock walls by quantitative electrical resistivity tomography (Zugspitze, German/Austrian Alps), J. Geophys. Res. - Earth Surface, 115, 1–15, 2010.

Kulatilake, P. H. S. W., Ucpirti, H., Wang, S., Radberg, G. and Stephansson, O.: Use of the distinct element method to perform stress analysis in rock with non-persistent joints and to study the effect of joint geometry parameters on the strength and deformability of rock masses, Rock Mech. Rock Eng., 25, 253–274, https://doi.org/10.1007/BF01041807, 1992.

Lepique, M.: Empfehlung Nr. 10 des Arbeitskreises 3.3 “Versuchstechnik Fels” der Deutschen Gesellschaft für Geotechnik e. V. Indirekter Zugversuch an Gesteinsproben – Spaltzugversuch, Bautechnik, 85, 623–627, https://doi.org/10.1002/bate.200810048, 2008.

Loke, M. H.: Res2Dinv. Geoelectrical Imaging 2D & 3D, Geotomo Software Sdn Bhd, 2019.

Mejía Camones, L. A., Vargas, E. d. A., Figueiredo, R. P. de and Velloso, R. Q.: Application of the discrete element method for modeling of rock crack propagation and coalescence in the step-path failure mechanism, Eng. Geol., 153, 80–94, https://doi.org/10.1016/j.enggeo.2012.11.013, 2013.

Mellor, M.: Mechanical properties of rocks at low temperatures, 2nd International Conference on Permafrost, Yakutsk, Siberia, 13-28 July, 1973.

Mutschler, T.: Neufassung der Empfehlung Nr. 1 des Arbeitskreises “Versuchstechnik Fels” der Deutschen Gesellschaft für Geotechnik e. V. Einaxiale Druckversuche an zylindrischen Gesteinsprüfkörpern, Bautechnik, 81, 825–834, https://doi.org/10.1002/bate.200490194, 2004.

Rode, M., Schnepfleitner, H. and Sass, O.: Simulation of moisture content in alpine rockwalls during freeze–thaw events, Earth Surf. Proc. Land., 41, 13, 1937–1950, https://doi.org/10.1002/esp.3961, 2016.

Schön, J. H.: Physical properties of rocks. Fundamentals and principles of petrophysics, Second Edition, Developments in Petroleum Science, Volume 65, Elsevier, Amsterdam, Oxford (UK), 2015.

Sass, O.: Rock moisture measurements. Techniques, results, and implications for weathering, Earth Surf. Proc. Land., 30, 3, 359–374, https://doi.org/10.1002/esp.1214, 2005.

Supper, R., Ottowitz, D., Jochum, B., Römer, A., Pfeiler, S., Kauer, S., Keuschnig, M. and Ita, A.: Geoelectrical monitoring of frozen ground and permafrost in alpine areas. Field studies and considerations towards an improved measuring technology, Near Surface Geophysics, 12, 93–115, https://doi.org/10.3997/1873-0604.2013057, 2014.

Telford, W. M., Geldart, L. P. and Sheriff, R. E.: Applied Geophysics, Second Edition, Cambridge University Press, Cambridge, 1990.

Tse, R. and Cruden, D. M.: Estimating joint roughness coefficients, Int. J. Rock Mech. Min., 16, 303–307, https://doi.org/10.1016/0148-9062(79)90241-9, 1979.

Ulusay, R.: The ISRM Suggested Methods for Rock Characterization, Testing and Monitoring: 2007-2014, Springer International Publishing, Cham, Heidelberg, New York, Dordrecht, London, 2015.

Yang, Z. Y., Lo, S. C. and Di, C. C.: Reassessing the Joint Roughness Coefficient (JRC) Estimation Using Z2, Rock Mech. Rock Eng., 34, 243–251, https://doi.org/10.1007/s006030170012, 2001.

Zhang, X.-P. and Wong, L. Ngai Yuen: Crack Initiation, Propagation and Coalescence in Rock-Like Material Containing Two Flaws. A Numerical Study Based on Bonded-Particle Model Approach, Rock Mech. Rock Eng., 46, 1001–1021, https://doi.org/10.1007/s00603-012-0323-1, 2013.

Zhang, K., Cao, P., Meng, J., Li, K. and Fan, W.: Modeling the Progressive Failure of Jointed Rock Slope Using Fracture Mechanics and the Strength Reduction Method, Rock Mech. Rock Eng., 48, 771–785, https://doi.org/10.1007/s00603-014-0605-x, 2015.